International Journal for Housing Science and Its Applications
Publish August 6, 2025. Volume 46, Issue 3 Pages 7685-7695

https,//doi.org/10.70517/ijhsa463659

# Exploration of single-side imaging technology for mass concrete structures based on three-dimensional laser scanning technology

**Yuan Feng[1], Yudi Wang[2,*], Xiujuan Liu[1], Yuanjun Zhang[1], Jiaye Wu[1], Zhigui Wu[1] and Xiaobin Lv[1]**
[1] Sichuan Central Inspection Technology Inc., Zigong, Sichuan, 643000, China
[2] China Institute of Water Resources and Hydropower Research, Beijing, 100048, China
Corresponding authors: (e-mail: yudiwang1119@163.com).

**Abstract** Massive concrete structures are widely used in construction projects, but their quality inspection faces technical bottlenecks. This study proposes a single-side imaging technique for mass concrete structures based on 3D laser scanning technology, which achieves accurate characterization of concrete structures through 3D laser point cloud acquisition, wavelet transform denoising and implicit surface reconstruction. The study firstly adopts 3D laser scanning technology for image acquisition, and applies the seed point 4-neighborhood grid distribution method to obtain the original image estimation; secondly, empirical mode decomposition is applied to measure the information of the scanned image; then wavelet transform processing is utilized to remove the noise and improve the quality of the data; finally, hole repair and surface reconstruction are realized through resampling, eigenface extraction and implicit surface construction. The experimental results show that, compared with RIEGL VUX-1UAV, the accuracy of this method is comparable in elevation difference measurement (the mean value of elevation difference is 0.019), but the point cloud density is improved by 2.75 times on average, and the average thickness of the point cloud at the edges is only 5.32 cm. Meanwhile, the method distributes the point cloud uniformly in the different thickness intervals, and the average proportion of the point cloud reaches 0.216, which ensures that the strength of the concrete structure is later stable growth, so that the strength assurance rate reaches 98.9% at a probability degree of 2.3. This technique provides an efficient and accurate solution for the inspection of mass concrete structures and can be widely used in the field of engineering quality assessment and monitoring.

**Index Terms** 3D laser scanning, mass concrete, single surface imaging, wavelet transform, implicit surface reconstruction, strength guarantee rate

## I. Introduction

Mass concrete is commonly used in bridges, tunnels, dams, large buildings and other engineering projects [1]. Due to the large size of the mass concrete structure, and the internal embedded dense reinforcing steel mesh, pre-embedded pipelines, concrete cooling pipes, etc., poor vibration and layered pouring time is too long and other factors are prone to cause defects such as honeycomb, segregation, lack of compaction and voids within the concrete structure [2]-[5]. Whether the construction quality of mass concrete structure is good or not is an important factor that affects the bearing capacity and durability of the superstructure [6]. Therefore, in order to ensure the long-term working performance of mass concrete structures, the detection and evaluation of its internal quality is crucial.

At the present stage, the concrete damage detection mostly adopts the visual detection method and some more primitive non-destructive testing methods, such as ultrasonic pulse method, pulse echo method, radar detection method, infrared thermal spectrum method, and acoustic emission method [7], [8]. These methods rely on the proficiency of workers, which not only consume a lot of manpower and material resources, but also have a great disadvantage in terms of precision and efficiency, and are unable to detect the subtle damage on the structural surface [9], [10]. In contrast, laser scanning, as a non-contact non-destructive testing method with the advantages of non-contact, broadband, high sensitivity, and high spatial resolution, is widely used for surface and buried defects in concrete structures [11]. It detects defects on the millimeter scale, or even on the micrometer scale, by accurately determining the laser displacement amplitude [12], [13]. Meanwhile, through the detection means of high-speed sweeping, combined with image processing methods as well as signal classification methods, the visualization that can be realized highlights the defect information, which significantly improves the digital and intelligent level of the quality inspection of concrete bond surface [14]-[16].

As an important part of modern construction projects, the quality detection and assessment of mass concrete structures is crucial to project safety. Currently, the detection of mass concrete structure mainly relies on traditional methods such as sampling detection and non-breakage detection, which have problems such as insufficient precision, low efficiency and limited detection range. Especially for large-scale water conservancy projects, bridges, tunnels and other key infrastructure, the traditional detection means has been difficult to meet the comprehensive, rapid and accurate detection needs. In recent years, with the increasing complexity and large-scale engineering structure, the concrete structure inspection technology has put forward higher requirements. Three-dimensional laser scanning technology has gradually become a research hotspot in the field of concrete structure inspection by virtue of its high precision, high resolution, high efficiency and other significant advantages. By emitting the laser and receiving the reflected signal, this technology can quickly obtain the three-dimensional coordinate information of the target object surface, forming a high-density point cloud data, which provides a possibility for the surface characterization of concrete structure. However, the application of 3D laser scanning in concrete structure inspection still faces many challenges, including large-scale point cloud data processing, noise interference, data holes, and image information extraction, which limit the practical application of this technology in the inspection of large volume concrete structures. Therefore, the development of efficient imaging techniques for mass concrete structures has become an important research direction in the current engineering inspection field.

In this study, a single-side imaging technique for mass concrete structures based on three-dimensional laser scanning technology is proposed to address the above problems. Firstly, high-precision image acquisition is carried out by 3D laser scanning technology, and the scanning template of the image is divided into pixel blocks by using the 4-neighborhood grid distribution method of seed points to obtain the original image estimation value; secondly, an empirical modal decomposition method is adopted to measure the information of the 3D laser scanning image of the large volume concrete; and then the wavelet transform technology is applied to denoise the large-scale laser scanning data effectively; Finally, the accurate reconstruction of one-sided surfaces of mass concrete structures is realized through the steps of hole detection and repair, eigenface extraction, coordinate system calculation and implicit surface construction.

# II. Concrete imaging based on 3D laser scanning technology

## *II. A. Image Acquisition and Information Measurement of Massive Concrete Structures*

### II. A. 1) Image Acquisition of Massive Concrete Based on 3D Laser Scanning

In order to design the large volume concrete informative model calculation based on three-dimensional laser scanning technology, it is necessary to firstly carry out the three-dimensional laser scanning image acquisition of the large volume concrete object, and carry out the edge enhancement processing of the acquired fuzzy laser scanning image to improve the accuracy of the information quantization processing. The 3D laser scanning image is disturbed by an additive noise term $\eta(x,y)$, and the image is detected with a laser $X$ ray beam to obtain the template pixel values of the original image, and the scanning template of the image is partitioned into pixel blocks of $3\times3$ by the method of 4-neighborhood mesh distribution of the seed points to obtain an estimation of $\hat{f}(x,y)$ of the original image, which is used in the Reconstruction of Massive Concrete Images, the statistical values of the laser scanned pixels of the image acquisition are obtained by vector quantization decomposition:

$$E\,\mathrm{int}(vi)=\frac{1}{2}\left(\partial i\left|d-\left|vi-vi-1\right|\right|^2+\beta i\left|vi-1+2vi+vi+1\right|^2\right) \tag{1}$$

Among them:

$$d=\frac{1}{n}\sum_{i=0}^{n-1}\left|vi-vi-1\right| \tag{2}$$

The $d$ of the above equation is the average distance between the laser scanning points, and the quantitative statistical value of the image feature distribution varies with the characteristics of $H$ and $\eta$, when the more information of $H$ and $\eta$, the obtained mass concrete informative feature estimation value $\hat{f}(x,y)$ will be closer to $f(x,y)$ [17]. The imaging space domain for template matching of mass concrete images is derived as:

$$g(x,y)=h(x,y)*f(x,y)+\eta(x,y) \tag{3}$$

where $h(x,y)$ is the gray-scale degradation function of the laser-scanned mass concrete image and the symbol * denotes convolution. According to the quantization weighting of the laser scanned image, the rotational invariant moments distributed along the scanning direction of the beam domain are obtained as:

$$g(x,y) = f(x,y) + \eta(x,y) \tag{4}$$

where $\eta(x,y)$ is an additive noise term, and in the case of only additive noise, an edge pixel estimate of the laser-scanned mass concrete image hair is obtained as $\hat{f}(x,y) = \beta F(x,y) + (1-\beta)m_l$, where $F(x,y)$ is the pixel value of the laser-scanned imaging of the mass concrete object at point $(x,y)$, $m_l$ is the gray level difference feature dimension, and let $\delta_l^2$ be the local variance of the laser-scanned imaging of the mass concrete object, $\delta_\eta^2$ be the noise variance, and $\beta = \max\left[\dfrac{\delta_l^2 - \delta_\eta^2}{\delta_l^2}, 0\right]$. The edge contour line $V(s)$ is discretized and segmented by adding window synchronization, and wavelet analysis and fuzzy algorithms are used to compensate the imaging luminance and extract the regional pixel feature points for the high-frequency and low-frequency portions of the signal, respectively, and segment $V(s)$ into $N$ points along $s$, and the edge contour filtering transfer function of the laser-scanned large volume concrete image is:

$$\hat{f}(x,y) = \begin{cases} g(x,y)-1, & if\ g(x,y) - \hat{f}_{Lec}(x,y) \geq t \\ g(x,y)+1, & if\ g(x,y) - \hat{f}_{Loc}(x,y) < t \\ g(x,y), & else \end{cases} \tag{5}$$

The fusion process is performed on the image pixel-level neighborhood paradigm, and the information measurements of the bulk concrete image acquisition are obtained by adaptive local noise reduction as:

$$g(x,y) = f(x,y) + \eta_m(x,y) \tag{6}$$

where $f(x,y)$ denotes the input image, $g(x,y)$ denotes the gray value of the output mass concrete image after 3D laser scanning, and $\eta_m(x,y)$ denotes the feature difference value between pixel points satisfying $\eta_m(x,y) \in \{-1,0,1\}$. Through the above processing, the image acquisition of large volume concrete based on 3D laser scanning is realized.

#### II. A. 2) 3D laser scanning information measurement of mass concrete

The empirical modal decomposition (EMD) method was used to discretize the 3D laser scanned images of mass concrete, and the transverse scanning and block scanning models were used for multi-granularity coarse pixel feature representation, and the modal function of the separated band information measurements of the feature points for each frame of the laser scanning was described as follows:

$$x(n) = \frac{1}{\sqrt{N}} \sum_{k=0}^{N-1} X(k) \exp\left(j2\pi kn / N\right), n = 0,1 \cdots N-1 \tag{7}$$

where $X(k)$ is the amplitude characteristic of the laser scanning frame, and $\exp\left(j2\pi kn / N\right)$ is the separation phase characteristic of the data in the two frames. The key frame feature extraction method is used for noise separation to realize the information measurement of 3D laser scanning of mass concrete, and the iterative process of information measurement is:

$$x(k+1) = f(x(k \mid k)) + O + V(k) \tag{8}$$

The scale of the information feature point measurement of the mass concrete is $a(a<1)$, when the gray level of the center pixel of the contour line neighborhood $\left(M \times M\right)$ of the laser scanning mass concrete image is lower than the threshold, the template of $3 \times 3$ is chosen to carry out the feature parametric decomposition of information fusion of the image to obtain the local coordinate system of the image feature control point for:

$$\begin{cases} x = R\sin\eta\cos\varphi & 0 \leq \varphi \leq 2\pi \\ y = R\sin\eta\sin\varphi & 0 \leq \eta \leq \pi \\ z = R\cos\eta & R = \dfrac{D}{2} \end{cases} \tag{9}$$

where $\eta$ denotes the rotation angle of the edge point template matching of the bulk concrete image, and $\varphi$ denotes the image gray scale pixel feature deviation, the irregular triangular mesh dissection of the bulk concrete image was performed to obtain the pixel level intensity of the 3D laser scanning image as:

$$D = \alpha \cdot l_{\max} = \alpha \cdot \max_{l \in \{x,y,z\}} \left( \max_{i \in N_{ngb}} (p_{ij}) - \min_{i \in N_{ngb}} (p_{ij}) \right) \tag{10}$$

where $\alpha$ is the gray value of the edge point, the gray potential $E_{con}$ of the bulk concrete image is obtained, and the pixel decomposition equation of state of the information presenting region of the laser image is described as obtained by the edge pixel feature reconstruction:

$$I(x) = J(x)t(x) + A(1 - t(x)) \tag{11}$$

where $A$ is the attenuation of the bulk concrete informatics modeling arithmetic, $t(x)$ is the imaging resolution, and $J(x)t(x)$ is the pixel-level intensity of the image vector quantization kernel space. The resulting 3D laser scanning information measurement equation for mass concrete is described as:

$$\begin{aligned} E_{image}(Vi) = -\big| & I(xi-1, yi+1) + 2I(xi, yi+1) + I(xi+1, yi+1) \\ & -I(xi-1, yi-1) - 2I(xi, yi-1) - I(xi+1, yi-1)\big| \\ & +I(xi+1, yi-1) + 2I(xi+1, yi) + I(xi+1, yi-1) \\ & -I(xi-1, yi-1) - 2I(xi-1, yi) - I(xi-1, yi+1)\big| \end{aligned} \tag{12}$$

In order not to lose the generality, the batch model is used for feature segmentation of laser-scanned mass concrete images, so that the normalized expression for the gradient value of the 3D laser scanning information measurement of mass concrete is:

$$K = \frac{(Grad - \min Grad)}{(\max Grad - \min Grad)} \tag{13}$$

The gradient value of the 3D laser scanning image calculated by the above method realizes the accurate measurement of the 3D laser scanning information of the mass concrete, and provides an accurate data base for constructing the informationization model of the mass concrete.

### *II. B.Denoising of large-scale laser scanning data*

Due to the role of laser scanning equipment and other factors, there are some noises in the original large-scale laser scanning data, and they reduce the quality of surface reconstruction, so this paper uses wavelet transform to remove the noise processing in the original large-scale laser scanning data in order to improve the effect of large-scale laser scanning surface reconstruction. Let $\psi(t) \in L^2(R)$, the Fourier transform of $\psi(t)$ is $\hat{\psi}(\tilde{\omega})$, and the wavelet transform operation can be carried out if $\hat{\psi}(\omega)$ satisfies the condition of Eq:

$$C_{\psi} = \int_R \frac{|\hat{\psi}(\omega)|^2}{|\omega|} d\omega < \infty \tag{14}$$

where $\hat{\psi}(t)$ is the mother wavelet.

Stretching and translating operations on $\psi(t)$ can be obtained:

$$\psi_{a,b}(t) = \frac{1}{\sqrt{|a|}} \psi\left(\frac{t-b}{a}\right), a, b \in R, a \neq 0 \tag{15}$$

where $\psi_{a,b}(t)$ is the wavelet sequence. $a$ and $b$ are the scaling and translation factors, respectively [18].

Let the original large-scale laser scanning data containing noise be:

$$s(t) = x(t) + n(t) \tag{16}$$

where $s(t)$ and $n(t)$ are real and noise signals, respectively.

Realizing the discrete transform on $s(t)$ produces $s(n)$, $n = 0, 1, 2, \cdots, N-1$, and the wavelet transform can be described as:

$$W_{2^j}s(k)=\frac{1}{2^j}\sum_{n=0}^{N-1}s(n)\psi^*(2^{-j}n-k)j,k\in Z \tag{17}$$

The scale and wavelet coefficients are $xf(j,k)$ and $Wf(j,k)$, respectively, and multiple wavelet subdivisions are performed by recursive operations of Eq:

$$\begin{aligned}xf(j+1,k)&=xf(j,k)*h(j,k)\\ Wf(j+1,k)&=xf(j,k)*g(j,k)\end{aligned} \tag{18}$$

where $xf(0,k)$ is the true signal. $h$ and $g$ are low-pass and high-pass filters.

The noise in the original large-scale laser scanning data is removed by setting a certain threshold, and finally the high-quality original large-scale laser scanning data is obtained by wavelet reconstruction, and the reconstruction formula is specified as:

$$xf(j-1,k)=xf(j,k)*h_0(j,k)+Wf(j,k)*g_0(j,k) \tag{19}$$

where $h_0$ and $g_0$ are the reconstructed low-pass and high-pass filters.

The original large-scale laser scanning data containing noise is denoised using wavelet transform [19].

## *II. C.One-sided surface reconstruction of mass concrete structures*

### II. C. 1) Detection and repair of holes

In the process of large-scale laser scanning surface reconstruction, some holes will be generated, which need to be repaired, and the detection of holes is the basis of hole repair. Let the point $P$ exists on the boundary, and all the feature points of the surface boundary are obtained according to the $K-$ neighboring points. According to the definition of boundary feature points, two types of holes can be obtained: closed holes and non-closed holes [20]. In order to repair the holes of the large-scale laser scanning cloud data comprehensively, the non-closed holes are firstly converted into closed holes and then repaired, the steps of converting non-closed holes into closed holes are:

Step1: Select multiple non-noise points as control vertices on the edges of the non-closed holes.

Step2: Perform curve boundary fitting operation on the control vertices.

Step3: Resample the curve boundary curve to get new sampling points.

Step4: Establish a new hole boundary based on the original boundary points and the new sample points.

If two neighboring points $P_i$ and $P_j$ are spaced $\Delta>\lambda\times\Delta_{\min}$, then additional sampling points are needed between $P_i$ and $P_j$, $\Delta=u_i-u_j$, $u_i$ and $u_j$ are parameter values associated with $P_i$ and $P_j$, respectively, there:

$$n=Int\left(\Delta/\left(\lambda\times\Delta_{\min}\right)\right) \tag{20}$$

$$u_i^*=u_i+\frac{\Delta}{n}\times i,i=1,\cdots,n-1 \tag{21}$$

where $n$ denotes the number of new sampling points between $P_i$ and $P_j$, and $u_i^*$ is the parameter value of the new sampling points.

### II. C. 2) Extraction of eigenfaces in the domain adjacent to the hole

In order to repair the hole more accurately, the feature surface of the hole region is extracted. The hole and the surrounding information is the hole neighborhood domain, and the thickness can describe how many points near the hole. Let the points between the hole and the proximity domain be $P_1,P_2,\cdots,P_n$, if the sum of squares of these points is minimized, then it means that they constitute the eigenfaces, and let the center of the shape of $P_1,P_2,\cdots,P_n$ be $O$, the eigenfacets can be described by spatial points $O$ and unit normal vectors $n$, then there are:

$$O=\frac{1}{n}\sum_{i=0}^{n}P_i \tag{22}$$

Then the corresponding construction matrix is:

$$M=\begin{bmatrix} P_1-O \\ P_2-O \\ \cdots\cdots\cdots \\ P_n-O \end{bmatrix} \tag{23}$$

**II. C. 3) Calculating the coordinate system of the hole**

Let $d\left(P_i,O\right)\geq d\left(P_j,O\right)$, $\forall j\neq i$, then $P_i$ denote the furthest point of $P_1,P_2,\cdots,P_n$, i.e. $P_d$, $d(x,y)$ is the distance between $x$ and $y$, $(P_d-O)\times n$, $n\times\left((P_d-O)\times n\right)$, and $n$ are the $u$, $v$, and $s$ axes of the coordinate system, which form the hole coordinate system.

**II. C. 4) Constructing implicit surfaces**

Let $U$ be a subdomain of the fitted region, then the fitting function is:

$$s(p)=\sum_{i=0}^{m}a_i(p)M_i(p)=M^T(p)a(p) \tag{24}$$

where $p\in U$ and $a(p)=[a_1(p),a_2(p),\cdots,a_m(p)]^{\mathrm{T}}$ are the coefficients to be solved. $M(p)$ is the basis function and the fitting function becomes:

$$s(p)=a_0(p)+a_1(p)u+a_2(p)v+a_3(p)u^2+a_4(p)uv+a_5(p)v^2 \tag{25}$$

The weighted discrete L2 paradigm is defined as follows:

$$\begin{aligned} J&=\sum_{i=1}^{N}w(p-p_i)(s(p)-f_i) \\ &=\sum_{i=1}^{N}w(p-p_i)(a_0(p)+a_1(p)u+a_2(p)v+a_3(p)u^2 \\ &+a_4(p)uv+a_5(p)v^2-f_i) \end{aligned} \tag{26}$$

where $f_i$ is the node value at $P=P_i$ and $w(p-p_i)$ is the weight function of $p_i$.

In order to solve for the coefficient $a(p)$, the derivation of $a$ is performed and $\frac{\partial J}{\partial a}=0$, then there are:

$$a=\left(p-p_i\right)^{-1}BWf \tag{27}$$

where the $B$ value is calculated as:

$$B=\begin{bmatrix} 1,\cdots,1 \\ u_1,\cdots,u_n \\ v_1,\cdots,v_n \\ u_1^2,\cdots,u_n^2 \\ v_1^2,\cdots,v_n^2 \\ u_1v_1,\cdots,u_nv_n \end{bmatrix} \tag{28}$$

The relationship between the weight function $w(p-p_i)$ and $\|p-p_i\|$ is a monotonically decreasing relationship, and thus $a=\left(BWB^T\right)^{-1}BWf$ of $w\left(p-p_i\right)$ varies with the change in the estimated point. The weight function is given by:

$$w_i(p)=\frac{e^{-\mu d_i^2(p)}}{d_i^2(p)} \tag{29}$$

The weight function is closely related to the resampling point, and the coefficients $a(p)$ are to be recalculated, i.e:

$$a(p)=\left(BW(p)B^T\right)^{-1}BW(p)f \tag{30}$$

where $W(p)$ is a diagonal take.

Steps to compute the functional equation of an implicit surface:

Step1: Project $P_1,P_2,\cdots,P_n$ onto the feature surface to obtain $s_1,s_2,\cdots,s$ in the hole coordinate system, and compute the $f$ vector values.

Step2: Project $P_1,P_2,\cdots,P_n$ onto the $u$ and $v$ axes, compute the coordinate values $u_1,u_2,\cdots,u_n$, $v_1,v_2,\cdots,v_n$, and obtain the value of $B$.

Step3: Obtain the weights of each point based on the resampled points and the projection points of $P_1,P_2,\cdots,P_n$ on the feature surface.

Step4: Calculate the coefficients $a_0$, $a_1$, $a_2$, $a_3$, $a_4$, $a_5$ of the solved fitted surfaces according to $B$, $W$, and $f$, and then calculate the surface functional equations of the re-sampled points to realize the surface reconstruction of large-scale laser description data.

# III. Experiments and analysis of results

## *III. A. Performance testing experiments*

The main purpose of the experiments in this section is to verify the actual scanning performance of the method in this paper. The performance of RIEGL VUX-1UAV and this paper's method is compared, and two kinds of mass concrete (A and B) are selected for the experiment, and the four indexes of the two methods, such as elevation difference, point cloud density, point cloud thickness, and point cloud penetration, are specifically compared and analyzed.

### III. A. 1) Comparison of RTK elevation values

The comparison of elevation difference is shown in Table 1.The mean value of the elevation difference between the laser point cloud scanned by RIEGL VUX-1UAV and the 18 field RTK points is 0.02.The mean value of the elevation difference between the laser point cloud scanned by the method of this paper and the 18 RTK points is 0.019.Therefore, the point cloud scanned by the method of this paper can reach the same accuracy of RIEGL VUX-1UAV.

Table 1: Elevation comparison

| RTK point | dZ | |
|---|---|---|
| | RIEGL VUX-1UAV | Ours |
| 1 | 0.0367 | 0.0199 |
| 2 | 0.0244 | 0.0086 |
| 3 | 0.0012 | -0.0214 |
| 4 | 0.0146 | -0.004 |
| 5 | -0.0031 | -0.0236 |
| 6 | 0.0136 | -0.006 |
| 7 | 0.0145 | -0.0159 |
| 8 | 0.0263 | 0.0091 |
| 9 | 0 | -0.0157 |
| 10 | -0.0155 | -0.0277 |
| 11 | -0.0462 | -0.0597 |
| 12 | 0.0234 | 0.0028 |
| 13 | 0.0379 | 0.0165 |
| 14 | 0.0436 | 0.0227 |
| 15 | -0.0128 | -0.029 |
| 16 | -0.0121 | -0.0163 |
| 17 | -0.0105 | -0.0226 |
| 18 | 0.0236 | 0.0216 |

#### III. A. 2) Point cloud density

The point cloud densities of the two methods in this experiment are mainly related to the field of view angle and the laser emission frequency, the actual field of view angles of the RIEGL VUX-1UAV and the method in this paper are 90° and 85°, respectively, and the laser emission frequencies are 550 kHz and 400 kHz, respectively, and the point cloud densities are shown in Table 2. The point cloud scanned by this paper's method has an average point cloud density of 2.75 times that of RIEGL VUX-1UAV in each selected area. Therefore, the method in this paper can obtain a higher point cloud density at a lower scanning frequency.

Table 2: Dot cloud density

| Area | RIEGL VUX-1UAV | Ours |
|---|---|---|
| $A_1$ | 119.26 | 320.83 |
| $A_2$ | 105.6 | 373.32 |
| $A_3$ | 89.82 | 320.57 |
| $A_4$ | 134.17 | 238.35 |
| $A_5$ | 120.7 | 200.76 |
| $B_1$ | 46.3 | 136.69 |
| $B_2$ | 50.33 | 98.14 |
| $B_3$ | 61.24 | 235.72 |
| $B_4$ | 73.24 | 392.21 |
| $B_5$ | 147.98 | 381.65 |
| $B_6$ | 142.34 | 304.07 |

#### III. A. 3) Point cloud thickness

The point cloud thickness of this paper's method is shown in Table 3. From the table, it can be seen that the point cloud thicknesses in this paper are all small, the average thickness of the point cloud at the right bottom is 3.68 cm, and the average thickness of the point cloud at the edge is 5.32 cm, which is good for the stability and reproducibility of the echo of the mass concrete structure.

Table 3: Dot cloud thickness (m)

| Area | RIEGL VUX-1UAV | Ours |
|---|---|---|
| $A_1$ | 0.022 | 0.035 |
| $A_2$ | 0.047 | 0.039 |
| $A_3$ | 0.043 | 0.035 |
| $A_4$ | 0.042 | 0.045 |
| $A_5$ | 0.026 | 0.03 |
| $B_1$ | 0.05 | 0.059 |
| $B_2$ | 0.051 | 0.062 |
| $B_3$ | 0.067 | 0.071 |
| $B_4$ | 0.04 | 0.039 |
| $B_5$ | 0.062 | 0.044 |
| $B_6$ | 0.049 | 0.044 |

#### III. A. 4) Point Cloud Penetration

The point cloud penetration is mainly related to the laser power, laser divergence angle and measurement distance, and both the RIEGL VUX-1UAV and the method in this paper have a laser class of 1 and a laser divergence angle of 0.5 mrad. In this experiment, two pieces of mass concrete $C_1$ and $C_2$ are selected to analyze the point cloud penetration, and the point cloud of each mass concrete is divided into five intervals H1~H5 according to the thickness.The point cloud penetration of each selected area is shown in Table 4. Analyzing the data, it can be seen that the point cloud penetration of both methods is better. The point cloud scanned by this paper's method is uniformly distributed in different thickness intervals, with better penetration, and the structure is more completely expressed, and the average percentage of the point cloud of this paper's method is 0.216, with better penetration of the point cloud, which still ensures a better quality of the point cloud while realizing efficient scanning.

Table 4: The various constituencies point cloud penetrability

| Area | Thickness range | RIEGL VUX-1UAV | | Ours | |
|---|---|---|---|---|---|
| | | Counts | Proportion | Counts | Proportion |
| $C_1$ | $T_1$ | 2359.9 | 0.11 | 11441.3 | 0.29 |
| | $T_2$ | 843.2 | 0.07 | 3228.8 | 0.12 |
| | $T_3$ | 1944.7 | 0.16 | 7392.9 | 0.19 |
| | $T_4$ | 4168.3 | 0.32 | 11920.6 | 0.29 |
| | $T_5$ | 4064.9 | 0.3 | 8264.1 | 0.21 |
| $C_2$ | $T_1$ | 1081.6 | 0.12 | 6355.5 | 0.28 |
| | $T_2$ | 549.7 | 0.09 | 1389.1 | 0.04 |
| | $T_3$ | 651.5 | 0.1 | 2733.8 | 0.13 |
| | $T_4$ | 1382.1 | 0.14 | 4682.9 | 0.19 |
| | $T_5$ | 4429.2 | 0.53 | 10982 | 0.42 |

### *III. B. Regular growth of late strength of mass concrete*

#### III. B. 1) Intensity normal distribution

The area between the curve and the horizontal coordinate represents the sum of the frequencies (probabilities) and is equal to 100%, the probability is the chance that the data obtained from the test will fall in the graph, which can be expressed by the distribution function, and the area of the normal distribution for different $\sigma$ value ranges is shown in Figure 1. The area in the range $x = \overline{f} - \sigma$ to $x = \overline{f} + \sigma$ is 67.9% of the total area. The area in the range $x = \overline{f} - 2\sigma$ to $x = \overline{f} + 2\sigma$ is 95.9% of the total area. The area in the range $x = \overline{f} - 3\sigma$ to $x = \overline{f} + 3\sigma$ is 98.9% of the total area.

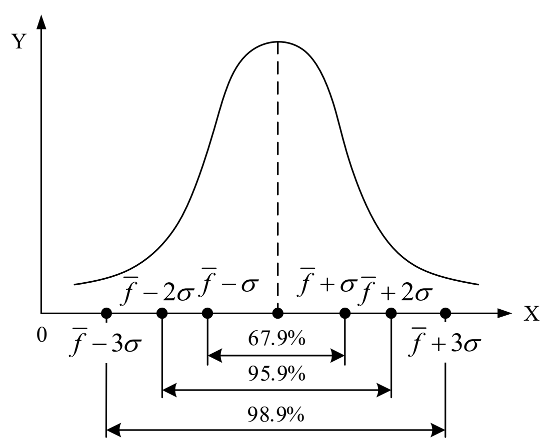


Figure 1: The area of the normal distribution

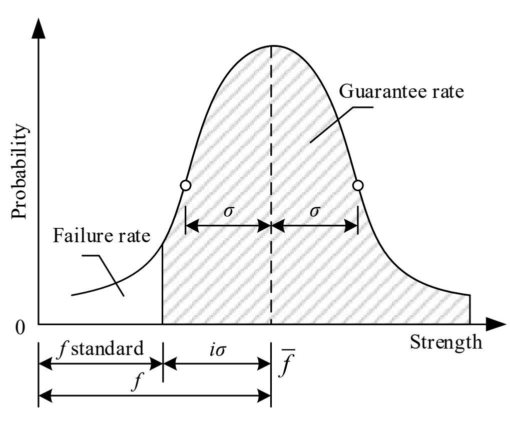


Figure 2: Strength assurance

**III. B. 2) Strength guarantee rate**

The strength guarantee ratio is the ratio of the shaded area in the figure to the total area in the figure, and this ratio is a good reflection of the strength guarantee ratio for the design strength class. The strength guarantee ratio is shown in Figure 2.

When calculating the strength guarantee rate $P$ for mass concrete, the probability degree $(t)$ (also known as the guarantee rate coefficient) is first calculated based on the design strength grade of mass concrete $(f_{cu.k})$, the average value of strength $(\overline{f})$, the coefficient of variation $(\delta)$ or the standard deviation $(\sigma)$.

$$t=\frac{\overline{f}-f_{cu.k}}{\sigma}=\frac{\overline{f}-f_{cu.k}}{\delta\cdot\overline{f}} \tag{31}$$

The guarantee rate can be found from the probability degree $t$ and then from the normal distribution curve equation. The strength assurance rate is shown in Table 5. It can be seen that, under the low temperature and cold conditions, strengthening the monitoring of the thermal insulation refers to the concrete, which indeed ensures the regular and effective growth of the strength of the concrete in the late stage.

Table 5: Strength assurance

| $t(ft/\sigma)$ | $P(\%)$ | $t(ft/\sigma)$ | $P(\%)$ | $t(ft/\sigma)$ | $P(\%)$ |
|---|---|---|---|---|---|
| 0.1 | 54.3 | 1.1 | 86.6 | 2.1 | 98.6 |
| 0.2 | 56.9 | 1.2 | 89.5 | 2.2 | 98.7 |
| 0.3 | 62.3 | 1.3 | 90.4 | 2.3 | 98.9 |
| 0.4 | 65.8 | 1.4 | 92.7 | 2.4 | 99.1 |
| 0.5 | 69.2 | 1.5 | 93.6 | 2.5 | 99.3 |
| 0.6 | 73.4 | 1.6 | 94.2 | 2.6 | 99.4 |
| 0.7 | 75.2 | 1.7 | 95.6 | 2.7 | 99.6 |
| 0.8 | 79.6 | 1.8 | 96.6 | 2.8 | 99.7 |
| 0.9 | 82.1 | 1.9 | 97.4 | 2.9 | 99.8 |
| 1 | 83.5 | 2 | 97.9 | 3 | 99 |

## IV. Conclusion

The following conclusions were obtained through the research and experimental analysis of the single-plane imaging technique for mass concrete structures based on 3D laser scanning technology:

The developed 3D laser scanning imaging method performs excellently in the inspection of mass concrete structures, and compared with the RIEGL VUX-1UAV scanning system, the mean value of the elevation difference between the laser point cloud scanned by this method and the RTK points is 0.019, which is comparable to the accuracy.

In terms of point cloud density, the point cloud density of the present method is on average 2.75 times higher than that of RIEGL VUX-1UAV in each selected area, and higher point cloud density is realized at lower scanning frequency. The point cloud thickness test shows that the average thickness of the point cloud of this method is 3.68 cm and 5.32 cm for the directly below and the edge, respectively, which is better for the concrete structure echo stability. The point cloud penetration test shows that the scanned point cloud of this method is uniformly distributed in different thickness intervals, with an average percentage of 0.216, which is good for penetration.

In addition, the analysis of the strength growth law of concrete in the later stage shows that the concrete strength guarantee rate can reach 98.9% when the probability degree reaches 2.3 through effective thermal insulation measures. These results show that the single-side imaging technology for mass concrete structures based on 3D laser scanning can efficiently and accurately obtain concrete structure information, provides technical innovation for engineering monitoring and assessment, and is suitable for quality inspection and assessment applications of large-scale engineering structures.

## Funding

The Open Research Fund project of the Key Laboratory of Water Engineering Materials of the Ministry of Water Resources (EMF202409).

## References

[1] Wang, Q., Ren, X., & Ballarini, R. (2020). A multifield model for early-age massive concrete structures: Hydration, damage, and creep. Journal of Engineering Mechanics, 146(10), 04020115.
[2] Fairbairn, E. M., & Azenha, M. (2019). Thermal cracking of massive concrete structures. State of Art Report of the RILEM TC.
[3] Attiyah, A. N., Al-Wazni, S., Al-Tameemi, A. A., & Al-Ansari, L. (2024). Structural evaluation of mass concrete damage: a case study of concrete mill stands. Journal of Building Pathology and Rehabilitation, 9(2), 149.
[4] Golewski, G. L. (2023). The phenomenon of cracking in cement concretes and reinforced concrete structures: the mechanism of cracks formation, causes of their initiation, types and places of occurrence, and methods of detection—a review. Buildings, 13(3), 765.
[5] Simos, N., Fallier, M., Joos, T., Johnson, E., & Soueid, A. (2020). Thermally induced cracking on the massive concrete structure of the NSLS II synchrotron and its engineering remediation. Engineering Structures, 212, 110519.
[6] Mechtcherine, V., Nerella, V. N., Will, F., Näther, M., Otto, J., & Krause, M. (2019). Large-scale digital concrete construction–CONPrint3D concept for on-site, monolithic 3D-printing. Automation in construction, 107, 102933.
[7] Yuan, C., Xiong, B., Li, X., Sang, X., & Kong, Q. (2022). A novel intelligent inspection robot with deep stereo vision for three-dimensional concrete damage detection and quantification. Structural health monitoring, 21(3), 788-802.
[8] Zhang, C., Chang, C. C., & Jamshidi, M. (2020). Concrete bridge surface damage detection using a single-stage detector. Computer-Aided Civil and Infrastructure Engineering, 35(4), 389-409.
[9] Kontoni, D. P. N., Kumar, A., Arora, H. C., Jahangir, H., & Kapoor, N. R. (2023). Damage detection in reinforced concrete structures using advanced automatic systems: An overview. Automation in Construction toward Resilience, 463-484.
[10] Jiang, Y., Pang, D., & Li, C. (2021). A deep learning approach for fast detection and classification of concrete damage. Automation in Construction, 128, 103785.
[11] Wang, Q., Sohn, H., & Cheng, J. C. (2018). Automatic as-built BIM creation of precast concrete bridge deck panels using laser scan data. Journal of Computing in Civil Engineering, 32(3), 04018011.
[12] Jang, K., & An, Y. K. (2018). Multiple crack evaluation on concrete using a line laser thermography scanning system. Smart Struct. Syst, 22(2), 201-207.
[13] Cho, S., Park, S., Cha, G., & Oh, T. (2018). Development of image processing for crack detection on concrete structures through terrestrial laser scanning associated with the octree structure. Applied Sciences, 8(12), 2373.
[14] Kim, M. K., Sohn, H., & Chang, C. C. (2015). Localization and quantification of concrete spalling defects using terrestrial laser scanning. Journal of Computing in Civil Engineering, 29(6), 04014086.
[15] Law, D. W., Silcock, D., & Holden, L. (2018). Terrestrial laser scanner assessment of deteriorating concrete structures. Structural Control and Health Monitoring, 25(5), e2156.
[16] Valença, J., Puente, I., Júlio, E. N. B. S., González-Jorge, H., & Arias-Sánchez, P. (2017). Assessment of cracks on concrete bridges using image processing supported by laser scanning survey. Construction and Building Materials, 146, 668-678.
[17] Haitao Lin,Hua Zhang,Yonglong Li,Jianwen Huo,Hao Deng & Huan Zhang. (2024). Method of 3D reconstruction of underwater concrete by laser line scanning. Optics and Lasers in Engineering,183,108468-108468.
[18] Sehyeon Yoon,Sanghyun Choi & Jhonghyun An. (2024). Effective Denoising Algorithms for Converting Indoor Blueprints Using a 3D Laser Scanner. Electronics,13(12),2275-2275.
[19] Hu Weiwei,Zhang Keke,Shao Lihuan,Lin Qinglei,Hua Yongzhu & Qin Jin. (2022). Clustering Denoising of 2D LiDAR Scanning in Indoor Environment Based on Keyframe Extraction.Sensors,23(1),18-18.
[20] Chéruel Anthony & Ben Ftima Mahdi. (2023). Unrestrained ASR volumetric expansion for mass concrete structures: Review and experimental investigation using 3d laser scanning. Construction and Building Materials,399.